

A Numerical Scheme for Non-Newtonian Fluids and Plastic Solids under the GPR Model

Haran Jackson^{a,**}, Nikos Nikiforakis^a

^a*Cavendish Laboratory, JJ Thomson Ave, Cambridge, UK, CB3 0HE*

Abstract

A method for modeling non-Newtonian fluids (dilatants and pseudoplastics) by a power law under the GPR model is presented, along with a new numerical scheme for solving this system. The scheme is also modified to solve the well-known corresponding system for power-law elasto-plastic solids.

The scheme is based on a temporal operator splitting, with the homogeneous system solved using a finite volume method based on a WENO reconstruction, and the temporal ODEs solved using an analytical approximate solution, presented here. The method is found to perform favorably against problems with known exact solutions, and existing third-party numerical solutions. It is simple to implement, and is currently the only publicly-available method for solving this modified version of the GPR model.

Keywords: Godunov-Peshkov-Romenski, GPR, Non-Newtonian, Plasticity, Operator Splitting

1. Introduction

1.1. Background

As presented in 1.2, the GPR model of continuum mechanics has been purported to represent an effective method to describe both fluids and solids within the same hyperbolic system of differential equations. From a practical perspective, the potential ramifications of this include: the simplification of software made for the simulation of phenomena involving different states of matter (as commented on in Jackson [14]); and the use of the vast array of effective numerical solvers designed for first-order hyperbolic systems. From a theoretical perspective: the GPR model cannot produce waves of infinite speed, unlike the parabolic Navier-Stokes equations; and the first-principles derivation of the mechanism by which viscous effects appear under the GPR model has been commented to be more appropriate than the more phenomenological viscous law appearing in the traditional Navier-Stokes formulation (see Peshkov et al. [22]).

Thus far, the GPR model has been solved for a wide array of different fluids (inviscid and viscous Newtonian) and solids (elastic and elastoplastic) (see Dumbser et al. [6], Boscheri et al. [4], Peshkov et al. [20, 22]). It has also been extended to incorporate the effects of electrodynamics (see Dumbser et al. [7]) and a general relativity (see Peshkov et al. [23]). It is yet to be formally extended to include non-Newtonian power-law fluids, however. A method for doing so is presented in Section 2. Building upon the work of Jackson [14] (in which a numerical scheme based upon a split solver was presented for non-Newtonian fluids and elastic solids under the GPR model) a numerical scheme is then presented in Section 3 for solving this new model, and it is adapted slightly to work also for elastoplastic power-law materials. The scheme is validated against several 1D and 2D tests in Section 4, with discussion presented in Section 5.

*Corresponding author

**Principal corresponding author

Email address: `hj305@cam.ac.uk` (Haran Jackson)

1.2. The GPR Model

The GPR model, first introduced in Peshkov and Romenski [21] - and expanded upon by Dumbser et al. [6] and Boscheri et al. [4] - takes the following form:

$$\frac{\partial \rho}{\partial t} + \frac{\partial (\rho v_k)}{\partial x_k} = 0 \quad (1a)$$

$$\frac{\partial (\rho v_i)}{\partial t} + \frac{\partial (\rho v_i v_k + p \delta_{ik} - \sigma_{ik})}{\partial x_k} = 0 \quad (1b)$$

$$\frac{\partial A_{ij}}{\partial t} + \frac{\partial (A_{ik} v_k)}{\partial x_j} + v_k \left(\frac{\partial A_{ij}}{\partial x_k} - \frac{\partial A_{ik}}{\partial x_j} \right) = -\frac{\psi_{ij}}{\theta_1} \quad (1c)$$

$$\frac{\partial (\rho J_i)}{\partial t} + \frac{\partial (\rho J_i v_k + T \delta_{ik})}{\partial x_k} = -\frac{\rho H_i}{\theta_2} \quad (1d)$$

$$\frac{\partial (\rho E)}{\partial t} + \frac{\partial (\rho E v_k + (p \delta_{ik} - \sigma_{ik}) v_i + q_k)}{\partial x_k} = 0 \quad (1e)$$

where θ_1 and θ_2 are positive scalar functions, and $\psi = \frac{\partial E}{\partial A}$ and $\mathbf{H} = \frac{\partial E}{\partial \mathbf{J}}$. The following definitions are given:

$$p = \rho^2 \left. \frac{\partial E}{\partial \rho} \right|_{s,A} \quad (2a)$$

$$\sigma = -\rho A^T \left. \frac{\partial E}{\partial A} \right|_{\rho,s} \quad (2b)$$

$$T = \left. \frac{\partial E}{\partial s} \right|_{\rho,A} \quad (2c)$$

$$\mathbf{q} = T \frac{\partial E}{\partial \mathbf{J}} \quad (2d)$$

To close the system, the EOS must be specified, from which the above quantities and the sources can be derived. E is the sum of the contributions of the energies at the molecular scale (microscale), the material element¹ scale (mesoscale), and the flow scale (macroscale):

$$E = E_1(\rho, s) + E_2(\rho, s, A, \mathbf{J}) + E_3(\mathbf{v}) \quad (3)$$

Here, as in previous studies, such as Dumbser et al. [6], Boscheri et al. [4], E_1 is taken to be either the ideal gas EOS, a shock Mie-Gruneisen EOS, or the EOS of nonlinear hyperelasticity Barton et al. [1].

E_2 has the following quadratic form:

$$E_2 = \frac{c_s(\rho, s)^2}{4} \|\text{dev}(G)\|_F^2 + \frac{c_t(\rho, s)^2}{2} \|\mathbf{J}\|^2 \quad (4)$$

c_s is the characteristic velocity of transverse perturbations. c_t is related to the characteristic velocity of propagation of heat waves²:

¹The concept of a *material element* corresponds to that of a fluid parcel from fluid dynamics, applied to both fluids and solids.

²Note that Dumbser et al. [6] denotes this variable by α , which is avoided here due to a clash with a parameter of one of the equations of state used.

$$c_h = \frac{c_t}{\rho} \sqrt{\frac{T}{c_v}} \quad (5)$$

In previous studies, c_t has been taken to be constant, as it will in this study.

$G = A^T A$ is the Gramian matrix of the distortion tensor, and $\text{dev}(G)$ is the deviator (trace-free part) of G :

$$\text{dev}(G) = G - \frac{1}{3} \text{tr}(G) I \quad (6)$$

E_3 is the usual specific kinetic energy per unit mass:

$$E_3 = \frac{1}{2} \|\mathbf{v}\|^2 \quad (7)$$

The following forms are taken:

$$\theta_1 = \frac{\tau_1 c_s^2}{3 |A|^{\frac{5}{3}}} \quad (8a)$$

$$\theta_2 = \tau_2 c_t^2 \frac{\rho T_0}{\rho_0 T} \quad (8b)$$

$$\tau_1 = \begin{cases} \frac{6\mu}{\rho_0 c_s^2} & \text{viscous fluids} \\ \tau_0 \left(\frac{\sigma_0}{\|\text{dev}(\sigma)\|_F} \right)^n & \text{elastoplastic solids} \end{cases} \quad (9a)$$

$$\tau_2 = \frac{\rho_0 \kappa}{T_0 c_t^2} \quad (9b)$$

The justification of these choices is that classical Navier–Stokes–Fourier theory is recovered in the stiff limit $\tau_1, \tau_2 \rightarrow 0$ (see Dumbser et al. [6]). The power law for elastoplastic solids is based on material from Barton et al. [2].

Finally, it is straightforward to verify that as a consequence of (2a), (2b), (2c), (2d), we have the following relations:

$$\sigma = -\rho c_s^2 G \text{dev}(G) \quad (10a)$$

$$\mathbf{q} = c_t^2 T \mathbf{J} \quad (10b)$$

$$-\frac{\psi}{\theta_1(\tau_1)} = -\frac{3}{\tau_1} |A|^{\frac{5}{3}} A \text{dev}(G) \quad (10c)$$

$$-\frac{\rho \mathbf{H}}{\theta_2(\tau_2)} = -\frac{T \rho_0}{T_0 \tau_2} \mathbf{J} \quad (10d)$$

The following constraint also holds (see Peshkov and Romenski [21]):

$$\det(A) = \frac{\rho}{\rho_0} \quad (11)$$

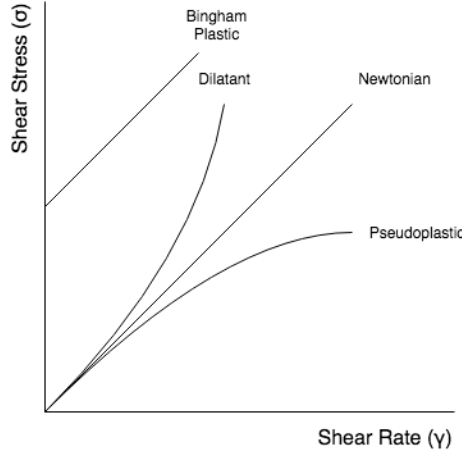


Figure 1: The stress-strain relationships for different kinds of fluids

The GPR model and Godunov and Romenski's 1970s model of elastoplastic deformation in fact relies upon the same equations. The realization of Peshkov and Romenski was that these are the equations of motion for an arbitrary continuum - not just a solid - and so the model can be applied to fluids too. Unlike in previous continuum models, material elements have not only finite size, but also internal structure, encoded in the distortion tensor.

The strain dissipation time τ_1 of the HPR model is a continuous analogue of Frenkel's "particle settled life time" (detailed in Frenkel [12]); the characteristic time taken for a particle to move by a distance of the same order of magnitude as the particle's size. Thus, τ_1 characterizes the time taken for a material element to rearrange with its neighbors. $\tau_1 = \infty$ for solids and $\tau_1 = 0$ for inviscid fluids. It is in this way that the HPR model seeks to describe all three major phases of matter, as long as a continuum description is appropriate for the material at hand.

The evolution equation for \mathbf{J} and its contribution to the energy of the system are derived from Romenski's model of hyperbolic heat transfer, originally proposed in Malyshev and Romenskii [17], Romenski [26], and implemented in Romenski et al. [25, 24]. In this model, \mathbf{J} is effectively defined as the variable conjugate to the entropy flux, in the sense that the latter is the derivative of the specific internal energy with respect to \mathbf{J} . Romenski remarks that it is more convenient to evolve \mathbf{J} and E than the heat flux or the entropy flux, and thus the equations take the form given here. τ_2 characterizes the speed of relaxation of the thermal impulse due to heat exchange between material elements.

2. Power-Law Fluids

The stress-strain relationships for various kinds of fluids are shown in Figure 1 on page 4. Dilatants and pseudoplastics may be modelled using the following power law, with $n > 1$ and $0 < n < 1$, respectively:

$$\boldsymbol{\sigma} = K |\dot{\boldsymbol{\gamma}}|^{n-1} \dot{\boldsymbol{\gamma}} \quad (12)$$

$$\dot{\boldsymbol{\gamma}} = \nabla \mathbf{v} + \nabla \mathbf{v}^T - \frac{2 \operatorname{tr}(\nabla \mathbf{v})}{3} \mathbf{I} \quad (13)$$

$K > 0$ is known as the *consistency*, and $K |\dot{\boldsymbol{\gamma}}|^{n-1}$ is the *apparent viscosity*. The norm is taken to be:

$$|X| = \sqrt{\frac{1}{2} X_{ij} X_{ij}} = \frac{\|X\|_F}{\sqrt{2}} \quad (14)$$

In Dumbser et al. [6] it was noted that when expressing the state variables as an asymptotic expansion in the relaxation parameter τ_1 , to first order we have:

$$\boldsymbol{\sigma} = \frac{1}{6} \tau_1 \rho_0 c_s^2 \left(\nabla \mathbf{v} + \nabla \mathbf{v}^T - \frac{2}{3} \text{tr}(\nabla \mathbf{v}) \mathbf{I} \right) \quad (15)$$

Thus, for a power law fluid, we require that:

$$\frac{1}{6} \tau_1 \rho_0 c_s^2 = K |\dot{\gamma}|^{n-1} \quad (16)$$

Taking moduli of both sides of (15), we also have:

$$|\boldsymbol{\sigma}| = \frac{1}{6} \tau_1 \rho_0 c_s^2 |\dot{\gamma}| \quad (17)$$

Combining these two relationships, we obtain:

$$\tau_1 = \frac{6K^{\frac{1}{n}}}{\rho_0 c_s^2} \left| \frac{1}{\boldsymbol{\sigma}} \right|^{\frac{1-n}{n}} := \tau_0 \left| \frac{1}{\boldsymbol{\sigma}} \right|^{\frac{1-n}{n}} \quad (18)$$

3. Numerical Scheme

Note that (1a), (1b), (1c), (1d), (1e) can be written in the following form:

$$\frac{\partial \mathbf{Q}}{\partial t} + \nabla \cdot \mathbf{F}(\mathbf{Q}) + \mathbf{B}(\mathbf{Q}) \cdot \nabla \mathbf{Q} = \mathbf{S}(\mathbf{Q}) \quad (19)$$

As described in Toro [28], a viable way to solve inhomogeneous systems of PDEs is to employ an operator splitting. That is, the following subsystems are solved:

$$\frac{\partial \mathbf{Q}}{\partial t} + \nabla \cdot \mathbf{F}(\mathbf{Q}) + \mathbf{B}(\mathbf{Q}) \cdot \nabla \mathbf{Q} = \mathbf{0} \quad (20a)$$

$$\frac{d\mathbf{Q}}{dt} = \mathbf{S}(\mathbf{Q}) \quad (20b)$$

The advantage of this approach is that specialized solvers can be employed to compute the results of the different subsystems. Let $H^{\delta t}, S^{\delta t}$ be the operators that take data $\mathbf{Q}(x, t)$ to $\mathbf{Q}(x, t + \delta t)$ under systems (20a) and (20b) respectively. A second-order scheme (in time) for solving the full set of PDEs over time step $[0, \Delta t]$ is obtained by calculating $\mathbf{Q}_{\Delta t}$ using a Strang splitting:

$$\mathbf{Q}_{\Delta t} = S^{\frac{\Delta t}{2}} H^{\Delta t} S^{\frac{\Delta t}{2}} \mathbf{Q}_0 \quad (21)$$

In the scheme proposed here, the homogeneous subsystem will be solved using a WENO reconstruction of the data, followed by a finite volume update, and the temporal ODEs will be solved with appropriate ODE solvers. This new scheme will be referred to here as *the Split-WENO method*.

Noting that $\frac{d\rho}{dt} = 0$ over the ODE time step, the operator S entails solving the following systems:

$$\frac{dA}{dt} = \frac{-3}{\tau_1} |A|^{\frac{5}{3}} A \operatorname{dev}(G) \quad (22a)$$

$$\frac{d\mathbf{J}}{dt} = -\frac{1}{\tau_2} \frac{T\rho_0}{T_0\rho} \mathbf{J} \quad (22b)$$

These systems can be solved concurrently with a stiff ODE solver. The Jacobians of these two systems to be used in an ODE solver are given in the appendix of Jackson [14]. However, these systems can also be solved separately, using the analytical results presented in 3.2 and 3.3, under specific assumptions. The second-order Strang splitting is then:

$$\mathbf{Q}_{\Delta t} = D^{\frac{\Delta t}{2}} T^{\frac{\Delta t}{2}} H^{\Delta t} T^{\frac{\Delta t}{2}} D^{\frac{\Delta t}{2}} \mathbf{Q}_0 \quad (23)$$

where $D^{\delta t}, T^{\delta t}$ are the operators solving the distortion and thermal impulse ODEs respectively, over time step δt . This allows us to bypass the relatively computationally costly process of solving these systems numerically.

3.1. The Homogeneous System

A WENO reconstruction of the cell-averaged data is performed at the start of the time step (as described in Dumbser et al. [10]). Focusing on a single cell C_i at time t_n , we have $\mathbf{w}^n(\mathbf{x}) = \mathbf{w}_p^n \Psi_p(\chi(\mathbf{x}))$ in C_i where Ψ_p is a tensor product of basis functions in each of the spatial dimensions. The flux in C is approximated by $\mathbf{F}(\mathbf{x}) \approx \mathbf{F}(\mathbf{w}_p) \Psi_p(\chi(\mathbf{x}))$. \mathbf{w}_p are stepped forwards half a time step using the update formula:

$$\begin{aligned} \frac{\mathbf{w}_p^{n+\frac{1}{2}} - \mathbf{w}_p^n}{\Delta t/2} = & -\mathbf{F}(\mathbf{w}_k^n) \cdot \nabla \Psi_k(\chi_p) \\ & - \mathbf{B}(\mathbf{w}_p^n) \cdot (\mathbf{w}_k^n \nabla \Psi_k(\chi_p)) \end{aligned} \quad (24)$$

i.e.

$$\mathbf{w}_p^{n+\frac{1}{2}} = \mathbf{w}_p^n - \frac{\Delta t}{2\Delta x} \begin{pmatrix} \mathbf{F}(\mathbf{w}_k^n) \cdot \nabla \Psi_k(\chi_p) \\ + \mathbf{B}(\mathbf{w}_p^n) \cdot (\mathbf{w}_k^n \nabla \Psi_k(\chi_p)) \end{pmatrix} \quad (25)$$

where χ_p is the node corresponding to Ψ_p . This evolution to the middle of the time step is similar to that used in the second-order MUSCL and SLIC schemes (see Toro [28]) and, as with those schemes, it is integral to giving the method presented here its second-order accuracy.

Integrating (20a) over C gives:

$$\mathbf{Q}_i^{n+1} = \mathbf{Q}_i^n - \Delta t_n \left(\mathbf{P}_i^{n+\frac{1}{2}} + \mathbf{D}_i^{n+\frac{1}{2}} \right) \quad (26)$$

where

$$\mathbf{Q}_i^n = \frac{1}{V} \int_C \mathbf{Q}(\mathbf{x}, t_n) d\mathbf{x} \quad (27a)$$

$$\mathbf{P}_i^{n+\frac{1}{2}} = \frac{1}{V} \int_C \mathbf{B} \left(\mathbf{Q} \left(\mathbf{x}, t_{n+\frac{1}{2}} \right) \right) \cdot \nabla \mathbf{Q} \left(\mathbf{x}, t_{n+\frac{1}{2}} \right) d\mathbf{x} \quad (27b)$$

$$\mathbf{D}_i^{n+\frac{1}{2}} = \frac{1}{V} \oint_{\partial C} \mathcal{D} \left(\mathbf{Q}^- \left(\mathbf{s}, t_{n+\frac{1}{2}} \right), \mathbf{Q}^+ \left(\mathbf{s}, t_{n+\frac{1}{2}} \right) \right) d\mathbf{s} \quad (27c)$$

where V is the volume of C and $\mathbf{Q}^-, \mathbf{Q}^+$ are the interior and exterior extrapolated states at the boundary of C , respectively.

Note that (20a) can be rewritten as:

$$\frac{\partial \mathbf{Q}}{\partial t} + \mathbf{M}(\mathbf{Q}) \cdot \nabla \mathbf{Q} = \mathbf{0} \quad (28)$$

where $\mathbf{M} = \frac{\partial \mathbf{F}}{\partial \mathbf{Q}} + \mathbf{B}$. Let \mathbf{n} be the normal to the boundary at point $\mathbf{s} \in \partial C$. For the GPR model, $\hat{\mathbf{M}} = \mathbf{M}(\mathbf{Q}(\mathbf{s})) \cdot \mathbf{n}$ is a diagonalizable matrix with decomposition $\hat{\mathbf{M}} = \hat{\mathbf{R}} \hat{\Lambda} \hat{\mathbf{R}}^{-1}$ where the columns of $\hat{\mathbf{R}}$ are the right eigenvectors and $\hat{\Lambda}$ is the diagonal matrix of eigenvalues. Define also $\hat{\mathbf{F}} = \mathbf{F} \cdot \mathbf{n}$ and $\hat{\mathbf{B}} = \mathbf{B} \cdot \mathbf{n}$. Using these definitions, the interface terms arising in the FV formula have the following form:

$$\begin{aligned} \mathcal{D}(\mathbf{Q}^-, \mathbf{Q}^+) &= \frac{1}{2} \left(\hat{\mathbf{F}}(\mathbf{Q}^+) + \hat{\mathbf{F}}(\mathbf{Q}^-) \right) \\ &\quad + \frac{1}{2} \left(+\tilde{\mathbf{B}}(\mathbf{Q}^+ - \mathbf{Q}^-) + \tilde{\mathbf{M}}(\mathbf{Q}^+ - \mathbf{Q}^-) \right) \end{aligned} \quad (29)$$

$\tilde{\mathbf{M}}$ is chosen to either correspond to a Rusanov/Lax-Friedrichs flux (see Toro [28]):

$$\tilde{\mathbf{M}} = \max \left(\max \left| \hat{\Lambda}(\mathbf{Q}^+) \right|, \max \left| \hat{\Lambda}(\mathbf{Q}^-) \right| \right) \quad (30)$$

or a Roe flux (see Dumbser and Toro [9]):

$$\hat{\mathbf{M}} = \left| \int_0^1 \mathbf{M}(\mathbf{q}^- + z(\mathbf{q}^+ - \mathbf{q}^-)) dz \right| \quad (31)$$

or a simplified Osher–Solomon flux (see Dumbser and Toro [9, 8]):

$$\tilde{\mathbf{M}} = \int_0^1 \left| \hat{\mathbf{M}}(\mathbf{Q}^- + z(\mathbf{Q}^+ - \mathbf{Q}^-)) \right| dz \quad (32)$$

where

$$\left| \hat{\mathbf{M}} \right| = \hat{\mathbf{R}} \left| \hat{\Lambda} \right| \hat{\mathbf{R}}^{-1} \quad (33)$$

$\tilde{\mathbf{B}}$ takes the following form:

$$\tilde{\mathbf{B}} = \int_0^1 \hat{\mathbf{B}}(\mathbf{Q}^- + z(\mathbf{Q}^+ - \mathbf{Q}^-)) dz \quad (34)$$

It was found that the Osher-Solomon flux would often produce slightly less diffusive results, but that it was more computationally expensive, and also had a greater tendency to introduce numerical artefacts.

$\mathbf{P}_i^{n+\frac{1}{2}}, \mathbf{D}_i^{n+\frac{1}{2}}$ are calculated using an $N + 1$ -point Gauss-Legendre quadrature, replacing $\mathbf{Q}\left(\mathbf{x}, t_{n+\frac{1}{2}}\right)$ with $\mathbf{w}^{n+\frac{1}{2}}(\mathbf{x})$.

3.2. The Thermal Impulse ODEs

Taking the EOS for the GPR model (3) and denoting by $E_2^{(A)}, E_2^{(J)}$ the components of E_2 depending on A and \mathbf{J} respectively, we have:

$$\begin{aligned} T &= \frac{E_1}{c_v} \\ &= \frac{E - E_2^{(A)}(\rho, s, A) - E_3(\mathbf{v})}{c_v} - \frac{1}{c_v} E_2^{(J)}(\mathbf{J}) \\ &= c_1 - c_2 \|\mathbf{J}\|^2 \end{aligned} \tag{35}$$

where:

$$c_1 = \frac{E - E_2^{(A)}(A) - E_3(\mathbf{v})}{c_v} \tag{36a}$$

$$c_2 = \frac{c_t^2}{2c_v} \tag{36b}$$

Over the time period of the ODE (22b), $c_1, c_2 > 0$ are constant. We have:

$$\frac{dJ_i}{dt} = - \left(\frac{1}{\tau_2} \frac{\rho_0}{T_0 \rho} \right) J_i \left(c_1 - c_2 \|\mathbf{J}\|^2 \right) \tag{37}$$

Therefore:

$$\frac{d}{dt} (J_i^2) = J_i^2 (-a + b (J_1^2 + J_2^2 + J_3^2)) \tag{38}$$

where

$$a = \frac{2\rho_0}{\tau_2 T_0 \rho c_v} \left(E - E_2^{(A)}(A) - E_3(\mathbf{v}) \right) \tag{39a}$$

$$b = \frac{\rho_0 c_t^2}{\tau_2 T_0 \rho c_v} \tag{39b}$$

Note that this is a generalized Lotka-Volterra system in $\{J_1^2, J_2^2, J_3^2\}$. It has the following analytical solution:

$$\mathbf{J}(t) = \mathbf{J}(0) \sqrt{\frac{1}{e^{at} - \frac{b}{a}(e^{at} - 1) \|\mathbf{J}(0)\|^2}} \tag{40}$$

3.3. The Distortion ODEs

3.3.1. Newtonian Fluids

Let $k_0 = \frac{3}{\tau_1} \left(\frac{\rho}{\rho_0} \right)^{\frac{5}{3}} > 0$ and let A have singular value decomposition $U\Sigma V^T$. Then:

$$G = (U\Sigma V^T)^T U\Sigma V^T = V\Sigma^2 V^T \quad (41)$$

$$\text{tr}(G) = \text{tr}(V\Sigma^2 V^T) = \text{tr}(\Sigma^2 V^T V) = \text{tr}(\Sigma^2) \quad (42)$$

Therefore:

$$\begin{aligned} \frac{dA}{dt} &= -k_0 U\Sigma V^T \left(V\Sigma^2 V^T - \frac{\text{tr}(\Sigma^2)}{3} I \right) \\ &= -k_0 U\Sigma \left(\Sigma^2 - \frac{\text{tr}(\Sigma^2)}{3} \right) V^T \\ &= -k_0 U\Sigma \text{dev}(\Sigma^2) V^T \end{aligned} \quad (43)$$

It is a common result (see Giles [13]) that:

$$d\Sigma = U^T dA V \quad (44)$$

and thus:

$$\frac{d\Sigma}{dt} = -k_0 \Sigma \text{dev}(\Sigma^2) \quad (45)$$

Using a fast 3×3 SVD algorithm (such as in McAdams et al. [18]), U, V, Σ can be obtained, after which the following procedure is applied to Σ , giving $A(t) = U\Sigma(t)V^T$.

Denote the singular values of A by a_1, a_2, a_3 . Then:

$$\Sigma \text{dev}(\Sigma^2) = \begin{pmatrix} a_1(a_1^2 - \alpha) & 0 & 0 \\ 0 & a_1(a_1^2 - \alpha) & 0 \\ 0 & 0 & a_1(a_1^2 - \alpha) \end{pmatrix} \quad (46)$$

where

$$\alpha = \frac{a_1^2 + a_2^2 + a_3^2}{3} \quad (47)$$

Letting $x_i = \frac{a_i^2}{\det(A)^{\frac{2}{3}}} = \frac{a_i^2}{\left(\frac{\rho}{\rho_0}\right)^{\frac{2}{3}}}$ we have:

$$\frac{dx_i}{d\tau} = -3x_i(x_i - \bar{x}) \quad (48)$$

where $\tau = \frac{2}{\tau_1} \left(\frac{\rho}{\rho_0} \right)^{\frac{7}{3}} t$ and \bar{x} is the arithmetic mean of x_1, x_2, x_3 . This ODE system travels along the surface $\Psi = \{x_1, x_2, x_3 > 0, x_1 x_2 x_3 = 1\}$ to the point $x_1, x_2, x_3 = 1$. This surface is symmetrical in the planes

$x_1 = x_2$, $x_1 = x_3$, $x_2 = x_3$. As such, given that the system is autonomous, the paths of evolution of the x_i cannot cross the intersections of these planes with Ψ . Thus, any non-strict inequality of the form $x_i \geq x_j \geq x_k$ is maintained for the whole history of the system. By considering (48) it is clear that in this case x_i is monotone decreasing, x_k is monotone increasing, and the time derivative of x_j may switch sign.

We now explore cases when even the reduced ODE system (48) need not be solved numerically. Define the following variables:

$$m = \frac{x_1 + x_2 + x_3}{3} \quad (49a)$$

$$u = \frac{(x_1 - x_2)^2 + (x_2 - x_3)^2 + (x_3 - x_1)^2}{3} \quad (49b)$$

It is a standard result that $m \geq \sqrt[3]{x_1 x_2 x_3}$. Thus, $m \geq 1$. Note that u is proportional to the internal energy contribution from the distortion. From (48) we have:

$$\frac{du}{d\tau} = -18 \left(1 - m \left(m^2 - \frac{5}{6}u \right) \right) \quad (50a)$$

$$\frac{dm}{d\tau} = -u \quad (50b)$$

Combining these equations, we have:

$$\frac{d^2 m}{d\tau^2} = -\frac{du}{d\tau} = 18 \left(1 - m \left(m^2 - \frac{5}{6}u \right) \right) \quad (51)$$

Therefore:

$$\begin{cases} \frac{d^2 m}{d\tau^2} + 15m \frac{dm}{d\tau} + 18(m^3 - 1) = 0 \\ m(0) = m_0 \\ m'(0) = -u_0 \end{cases} \quad (52)$$

We make the following assumption, noting that it is true in all physical situations tested in this study:

$$m(t) = 1 + \eta(t), \quad \eta \ll 1 \quad \forall t \geq 0 \quad (53)$$

Thus, we have the linearized ODE:

$$\begin{cases} \frac{d^2 \eta}{d\tau^2} + 15 \frac{d\eta}{d\tau} + 54\eta = 0 \\ \eta(0) = m_0 - 1 \\ \eta'(0) = -u_0 \end{cases} \quad (54)$$

This is a Sturm-Liouville equation with solution:

$$\eta(\tau) = \frac{e^{-9\tau}}{3} (ae^{3\tau} - b) \quad (55)$$

where

$$a = 9m_0 - u_0 - 9 \quad (56a)$$

$$b = 6m_0 - u_0 - 6 \quad (56b)$$

Thus, we also have:

$$u(\tau) = e^{-9\tau} (2ae^{3\tau} - 3b) \quad (57)$$

Denote the following:

$$m_{\Delta t} = 1 + \eta \left(\frac{2}{\tau_1} \left(\frac{\rho}{\rho_0} \right)^{\frac{7}{3}} \Delta t \right) \quad (58a)$$

$$u_{\Delta t} = u \left(\frac{2}{\tau_1} \left(\frac{\rho}{\rho_0} \right)^{\frac{7}{3}} \Delta t \right) \quad (58b)$$

Once these have been found, we have:

$$\frac{x_i + x_j + x_k}{3} = m_{\Delta t} \quad (59a)$$

$$\frac{(x_i - x_j)^2 + (x_j - x_k)^2 + (x_k - x_i)^2}{3} = u_{\Delta t} \quad (59b)$$

$$x_i x_j x_k = 1 \quad (59c)$$

This gives:

$$x_i = \frac{\Xi}{6} + \frac{u_{\Delta t}}{\Xi} + m_{\Delta t} \quad (60a)$$

$$x_j = \frac{1}{2} \left(\sqrt{\frac{x_i (3m_{\Delta t} - x_i)^2 - 4}{x_i}} + 3m_{\Delta t} - x_i \right) \quad (60b)$$

$$x_k = \frac{1}{x_i x_j} \quad (60c)$$

where

$$\Xi = \sqrt[3]{6 \left(\sqrt{81\Delta^2 - 6u_{\Delta t}^3} + 9\Delta \right)} \quad (61a)$$

$$\Delta = -2m_{\Delta t}^3 + m_{\Delta t} u_{\Delta t} + 2 \quad (61b)$$

Note that taking the real parts of the above expression for x_i gives:

$$x_i = \frac{\sqrt{6u_{\Delta t}}}{3} \cos\left(\frac{\theta}{3}\right) + m_{\Delta t} \quad (62a)$$

$$\theta = \tan^{-1}\left(\frac{\sqrt{6u_{\Delta t}^3 - 81\Delta^2}}{9\Delta}\right) \quad (62b)$$

At this point it is not clear which values of $\{x_i, x_j, x_k\}$ are taken by x_1, x_2, x_3 . However, this can be inferred from the fact that any relation $x_i \geq x_j \geq x_k$ is maintained over the lifetime of the system. Thus, the stiff ODE solver has been obviated by a few arithmetic operations.

3.3.2. Power Law Fluids

Take the singular value decomposition $A = U\Sigma V^T$. Note that:

$$\sigma = -\rho c_s^2 A^T A \operatorname{dev}(A^T A) = -\rho c_s^2 V \Sigma^2 \operatorname{dev}(\Sigma^2) V^T \quad (63)$$

Thus:

$$\|\sigma\|_F^k = \rho^k c_s^{2k} \|\Sigma^2 \operatorname{dev}(\Sigma^2)\|_F^k \quad (64)$$

Thus, according to (18), and letting $k = \frac{1-n}{n}$, we have:

$$\frac{d\Sigma}{dt} = -\frac{3}{\tau_0} \left(\frac{\rho}{\rho_0}\right)^{\frac{5}{3}} \frac{\rho^k c_s^{2k}}{2^{\frac{k}{2}}} \|\Sigma^2 \operatorname{dev}(\Sigma^2)\|_F^k \Sigma \operatorname{dev}(\Sigma^2) \quad (65)$$

Letting $x_i = \frac{a_i^2}{\det(A)^{\frac{2}{3}}} = \frac{a_i^2}{\left(\frac{\rho}{\rho_0}\right)^{\frac{2}{3}}}$ then $\Sigma^2 = \det(A)^{\frac{2}{3}} X$ where $X = \operatorname{diag}(x_1, x_2, x_3)$. Thus, we have:

$$\frac{dx_i}{dt} = -3 \|X \operatorname{dev}(X)\|_F^k x_i (x_i - \bar{x}) \quad (66)$$

where:

$$\tilde{t} = \frac{2}{\tau_0} \left(\frac{\rho}{\rho_0}\right)^{\frac{4k+7}{3}} \left(\frac{\rho c_s^2}{\sqrt{2}}\right)^k t \quad (67)$$

Note that:

$$\begin{aligned} 9 \|X \operatorname{dev}(X)\|_F^2 &= 4(x_1^4 + x_2^4 + x_3^4) \\ &\quad - 2(x_1^2 x_2^2 + x_3^2 x_2^2 + x_1^2 x_3^2) \\ &\quad + \sum_{i \neq j, j \neq k, k \neq i} x_i^2 x_j x_k - 4 \sum_{i \neq j} x_i^3 x_j \end{aligned} \quad (68)$$

Defining m, u as before, we have:

$$\|X \operatorname{dev}(X)\|_F^2 = \frac{1}{2} u^2 + 4m^2 u - 6m^4 + 6m \quad (69)$$

This leads to the following coupled system of ODEs:

$$\frac{du}{d\tilde{t}} = -18 \frac{d\tau}{d\tilde{t}} \left(1 - m \left(m^2 - \frac{5}{6} u \right) \right) \quad (70a)$$

$$\frac{dm}{d\tilde{t}} = -\frac{d\tau}{d\tilde{t}} u \quad (70b)$$

where we have defined the variable τ by:

$$\frac{d\tau}{d\tilde{t}} = \left(\frac{1}{2} u^2 + 4m^2 u - 6m^4 + 6m \right)^{\frac{k}{2}} \quad (71)$$

Using the approximation solution from before:

$$m(\tau) = 1 + \frac{e^{-9\tau}}{3} (ae^{3\tau} - b) \quad (72a)$$

$$u(\tau) = e^{-9\tau} (2ae^{3\tau} - 3b) \quad (72b)$$

It is straightforward to verify that:

$$\begin{aligned} \frac{d\tau}{d\tilde{t}} &= \frac{1}{54^{\frac{k}{2}}} \left(\begin{array}{c} 108ae^{-6\tau} - 324be^{-9\tau} \\ + 180a^2e^{-12\tau} - 612abe^{-15\tau} \\ + 459b^2e^{-18\tau} - 24a^2be^{-21\tau} \\ + (48ab^2 - 4a^4)e^{-24\tau} \\ + (16a^3b - 24b^3)e^{-27\tau} \\ - 24a^2b^2e^{-30\tau} + 16ab^3e^{-33\tau} \\ - 4b^4e^{-36\tau} \end{array} \right)^{\frac{k}{2}} \\ &\equiv \frac{f(\tau)^{\frac{k}{2}}}{54^{\frac{k}{2}}} \end{aligned} \quad (73)$$

$f(\tau)$ is approximated by $g(\tau) \equiv ce^{-\frac{c}{\lambda}\tau}$, where:

$$c = 108a - 324b + 180a^2 - 612ab + 459b^2 \quad (74a)$$

$$\begin{aligned} &- 24(a^2b - 2ab^2 + b^3) - 4(a - b)^4 \\ \lambda &= 18a - 36b + 15a^2 - \frac{204ab}{5} + \frac{51b^2}{2} \\ &- \frac{8a^2b}{7} + 2ab^2 - \frac{8b^3}{9} - \frac{a^4}{6} + \frac{16a^3b}{27} \\ &- \frac{4a^2b^2}{5} + \frac{16ab^3}{33} - \frac{b^4}{9} \end{aligned} \quad (74b)$$

Note that $f(0) = g(0)$ and $\int_0^\infty (f(\tau) - g(\tau)) d\tau = 0$. Thus, we have:

$$\frac{d\tau}{d\tilde{t}} \approx \left(\frac{c}{54} \right)^{\frac{k}{2}} e^{-\frac{kc}{2\lambda}\tau} \quad (75)$$

Therefore:

$$\begin{aligned}\tau &\approx \frac{2\lambda}{kc} \log \left(\frac{kc}{2\lambda} \left(\frac{c}{54} \right)^{\frac{k}{2}} \tilde{t} + 1 \right) \\ &= \frac{2\lambda}{kc} \log \left(\frac{kc}{\tau_0 \lambda} \left(\frac{\rho}{\rho_0} \right)^{\frac{4k+7}{3}} \left(\frac{\sqrt{c} \rho c_s^2}{6\sqrt{3}} \right)^k t + 1 \right)\end{aligned}\quad (76)$$

3.3.3. Elastoplastic Solids

For elastoplastic materials governed by the power law described in (9a):

$$\frac{d\Sigma}{dt} = -\frac{3}{\tau_0} \left(\frac{\rho}{\rho_0} \right)^{\frac{5}{3}} \frac{\left(\frac{3}{2} \right)^{\frac{n}{2}} \rho^n c_s^{2n} \|\text{dev}(\Sigma^2 \text{dev}(\Sigma^2))\|_F^n}{\sigma_0^n} \Sigma \text{dev}(\Sigma^2) \quad (77)$$

Thus, we have:

$$\frac{dx_i}{dt} = -3 \|\text{dev}(X \text{dev}(X))\|_F^n x_i (x_i - \bar{x}) \quad (78)$$

where:

$$\tilde{t} = \frac{2}{\tau_0} \left(\frac{\rho}{\rho_0} \right)^{\frac{4n+7}{3}} \left(\sqrt{\frac{3}{2}} \frac{\rho c_s^2}{\sigma_0} \right)^n t \quad (79)$$

Note that:

$$\begin{aligned}\frac{27}{2} \|\text{dev}(X \text{dev}(X))\|_F^2 &= \frac{3}{2} \sum_{i \neq j, j \neq k, k \neq i} x_i^2 x_j x_k \\ &\quad - 2 \sum_{i \neq j} x_i^3 x_j \\ &\quad - 3(x_1^2 x_2^2 + x_3^2 x_2^2 + x_1^2 x_3^2) \\ &\quad + 4(x_1^4 + x_2^4 + x_3^4)\end{aligned}\quad (80)$$

Thus we have:

$$\|\text{dev}(X \text{dev}(X))\|_F^2 = \frac{1}{6} u^2 + 4m^2 u - 6m^4 + 6m \quad (81)$$

This leads to the following coupled system of ODEs:

$$\frac{du}{d\tilde{t}} = -18 \frac{d\tau}{d\tilde{t}} \left(1 - m \left(m^2 - \frac{5}{6} u \right) \right) \quad (82a)$$

$$\frac{dm}{d\tilde{t}} = -\frac{d\tau}{d\tilde{t}} u \quad (82b)$$

where we have defined the variable τ by:

$$\frac{d\tau}{d\tilde{t}} = \left(\frac{1}{6}u^2 + 4m^2u - 6m^4 + 6m \right)^{\frac{n}{2}} \quad (83)$$

Then we have:

$$\frac{du}{d\tau} = -18 \left(1 - m \left(m^2 - \frac{5}{6}u \right) \right) \quad (84a)$$

$$\frac{dm}{d\tau} = -u \quad (84b)$$

Using the approximate solution (72a)(72b) again, it is straightforward to verify that:

$$\begin{aligned} \frac{d\tau}{d\tilde{t}} &= \frac{1}{54^{\frac{n}{2}}} \left(\begin{array}{c} 108ae^{-6\tau} - 324be^{-9\tau} \\ +108a^2e^{-12\tau} - 396abe^{-15\tau} \\ +297b^2e^{-18\tau} - 24a^2be^{-21\tau} \\ + (48ab^2 - 4a^4)e^{-24\tau} \\ + (16a^3b - 24b^3)e^{-27\tau} \\ -24a^2b^2e^{-30\tau} + 16ab^3e^{-33\tau} \\ -4b^4e^{-36\tau} \end{array} \right)^{\frac{n}{2}} \\ &\equiv \frac{f(\tau)^{\frac{n}{2}}}{54^{\frac{n}{2}}} \end{aligned} \quad (85)$$

$f(\tau)$ is approximated by $g(\tau) \equiv ce^{-\lambda\tau}$, where:

$$c = 108a - 324b + 108a^2 - 396ab + 297b^2 - 24(a^2b - 2ab^2 + b^3) - 4(a - b)^4 \quad (86a)$$

$$\begin{aligned} \lambda &= 18a - 36b + 9a^2 - \frac{132ab}{5} + \frac{33b^2}{2} \\ &\quad - \frac{8a^2b}{7} + 2ab^2 - \frac{8b^3}{9} - \frac{a^4}{6} \\ &\quad + \frac{16a^3b}{27} - \frac{4a^2b^2}{5} + \frac{16ab^3}{33} - \frac{b^4}{9} \end{aligned} \quad (86b)$$

Note that $f(0) = g(0)$ and $\int_0^\infty (f(\tau) - g(\tau)) d\tau = 0$. Thus, we have:

$$\frac{d\tau}{d\tilde{t}} \approx \left(\frac{c}{54} \right)^{\frac{n}{2}} e^{-\frac{nc}{2\lambda}\tau} \quad (87)$$

Therefore:

$$\begin{aligned} \tau &\approx \frac{2\lambda}{nc} \log \left(\frac{nc}{2\lambda} \left(\frac{c}{54} \right)^{\frac{n}{2}} \tilde{t} + 1 \right) \\ &= \frac{2\lambda}{nc} \log \left(\frac{nc}{\tau_0\lambda} \left(\frac{\rho}{\rho_0} \right)^{\frac{4n+7}{3}} \left(\frac{\sqrt{c}}{6} \frac{\rho c_s^2}{\sigma_0} \right)^n t + 1 \right) \end{aligned} \quad (88)$$

Thus, the value of A at time Δt is found by substituting the following into (72a),(72b):

$$\tau = \frac{2\lambda}{nc} \log \left(\frac{nc}{\tau_0 \lambda} \left(\frac{\rho}{\rho_0} \right)^{\frac{4n+7}{3}} \left(\frac{\sqrt{c}}{6} \frac{\rho c_s^2}{\sigma_0} \right)^n \Delta t + 1 \right) \quad (89)$$

The results are in turn substituted into (62a), (60b), (60c).

3.4. Distortion Correction in Fluids

Owing to the linearization step in (54), the method presented will perform poorly if the mean of the normalized singular values of the distortion tensor, m , deviates significantly from 1. To avert this, the following resetting procedure was applied globally for fluid flow problems when $m > 1.03$:

$$E \mapsto E - \frac{c_s^2}{4} \|\text{dev}(G)\|_F^2 \quad (90a)$$

$$A \mapsto \left(\frac{\rho}{\rho_0} \right)^{1/3} I \quad (90b)$$

This is justified by the fact that the distortion tensor is not a macroscopically-measurable quantity. This transformation leaves the density, pressure, and velocity of the fluid unchanged, and was found to improve the stability of the numerical scheme, while at the same time producing correct results, as demonstrated in the following section.

4. Numerical Results

4.1. Strain Relaxation Test

Take initial data used by Barton:

$$A = \begin{pmatrix} 1 & 0 & 0 \\ -0.01 & 0.95 & 0.02 \\ -0.015 & 0 & 0.9 \end{pmatrix}^{-1} \quad (91)$$

The following parameter values were used: $\rho_0 = 1, c_s = 0.219, n = 4, \sigma_0 = 9 \times 10^{-4}, \tau_0 = 0.1$. As can be seen in Figure 2 on page 17, Figure 3 on page 17, and Figure 4 on page 17, the approximate analytic solver compares well with the exact solution for the distortion tensor A , and thus also the stress tensor and the energy.

4.2. Poiseuille Flow

This test consists of a fluid traveling down a channel of constant width L , with a constant pressure gradient Δp along the length of the channel. No-slip boundary conditions are imposed on the channel walls. For a non-Newtonian fluid obeying a power law, the steady-state velocity profile across the channel is given by Ferras et al. [11]:

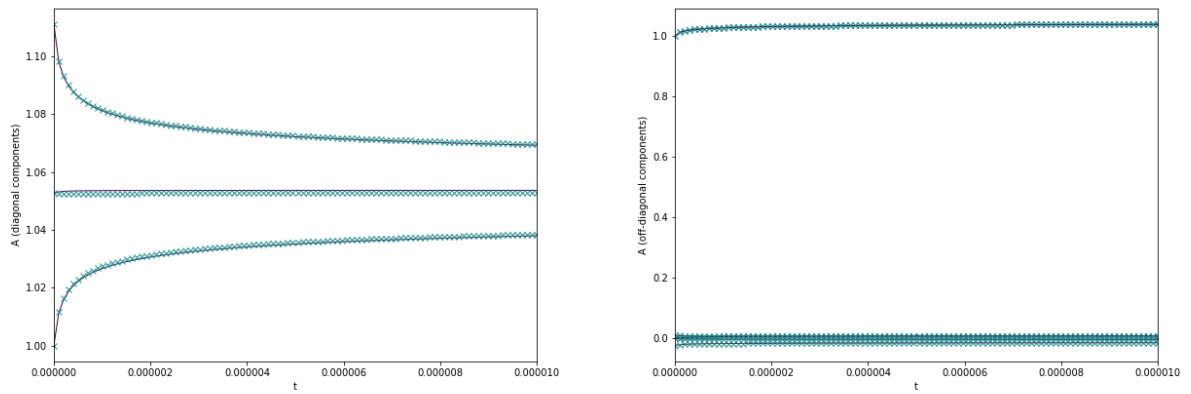


Figure 2: The distortion tensor during the Strain Relaxation Test

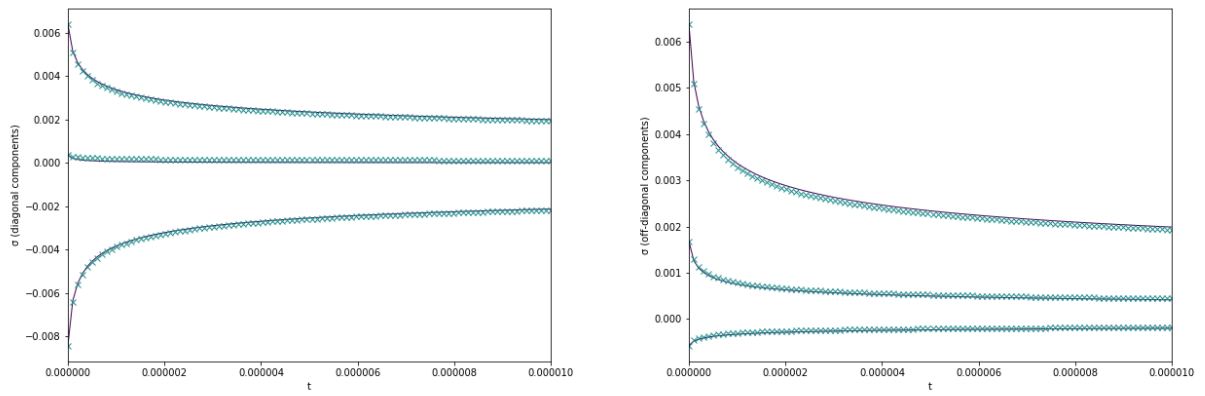


Figure 3: The stress tensor during the Strain Relaxation Test

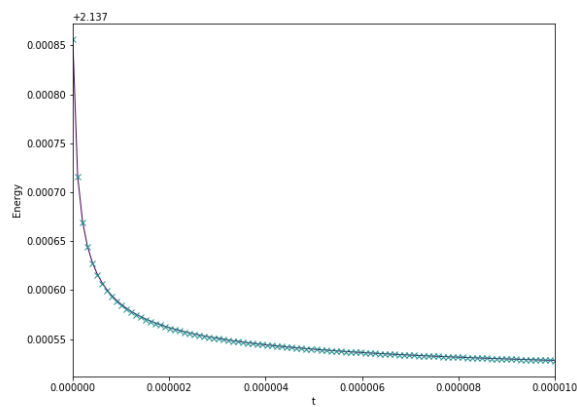


Figure 4: The total energy during the Strain Relaxation Test

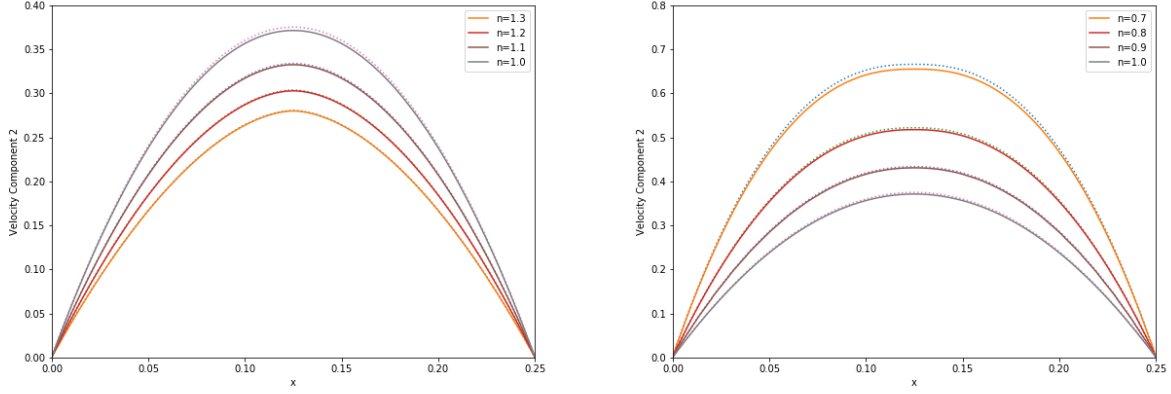


Figure 5: Velocity profiles for different dilatants (left) and pseudoplastics (right), in steady Poiseuille flow

$$v = \frac{\rho}{k} \left(\frac{\Delta p}{K} \right)^{1/n} \left(\left(\frac{L}{2} \right)^k - \left(x - \frac{L}{2} \right)^k \right) \quad (92a)$$

$$k = \frac{n+1}{n} \quad (92b)$$

where $x \in [0, L]$.

In this case, $L = 0.25$, $\Delta p = 0.48$, $K = 10^{-2}$. The fluid is initially at rest, with $\rho_0 = 1$, $A = I$, $p = 100/\gamma$. It follows an ideal gas EOS with $\gamma = 1.4$, $c_s = 1$. The pressure gradient is imposed by means of a body force, implemented as a constant source term to the momentum equation. The final time was taken to be 20, with 100 cells taken across the width of the channel.

Results for various values of n are shown in Figure 5 on page 18. The exact solutions are shown as dotted lines, with the numerical solutions in solid colors.

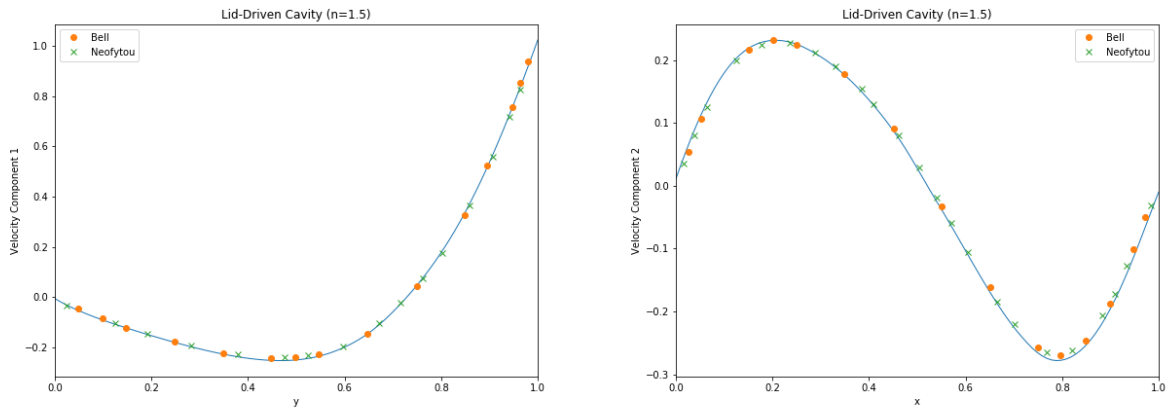
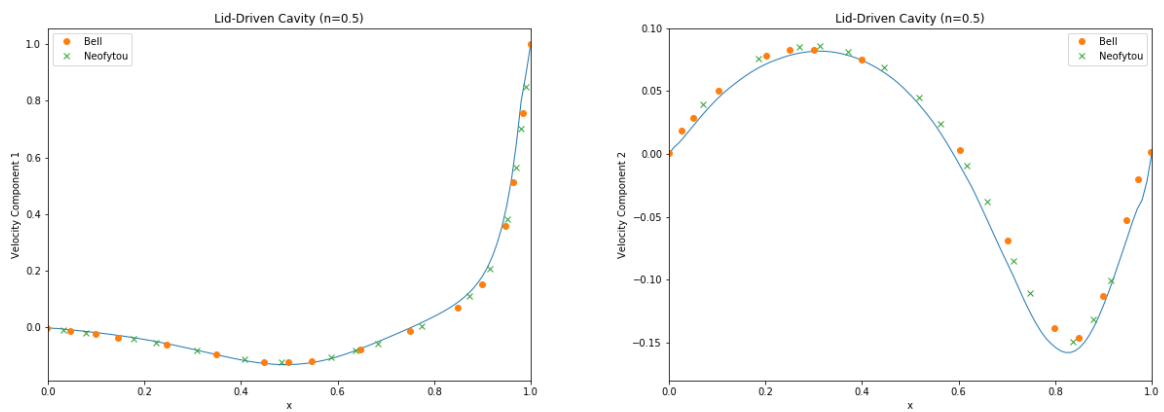
4.3. Lid-Driven Cavity

As detailed in Sverdrup et al. [27], this test consists of a square grid, with one side at a constant velocity of 1, and the other three stationary, with no-slip boundary conditions imposed. Here, the grid is chosen to have size 100×100 . The fluid obeys an ideal gas EOS with $\gamma = 1.4$, and a viscosity power law with $K = 10^{-2}$, for various n . We have $c_s = 1$. It is initially at rest, with $\rho = 1$, $p = 1$, $A = I$.

Figure 6 on page 19 and Figure 7 on page 19 show the results of running the system to steady state, for $n = 1.5$ and $n = 0.5$, respectively. The results are compared with those of Bell and Surana [3] and Neofytou [19]. As can be seen, there is very good agreement for the case $n = 1.5$, with the split solver performing slightly less well for the case $n = 0.5$. The 2D streamline plots found in Figure 8 on page 20 take the characteristic forms found in the aforementioned literature.

4.4. Elastoplastic Piston

This test is taken from Peshkov et al. [20], with exact solutions found in Maire et al. [16]. In this test, a piston with speed 20ms^{-1} is driven into copper initially at rest. An elastic shock wave develops, followed

Figure 6: Velocity profiles for the Lid-Driven Cavity Test, for a dilatant with $n=1.5$ Figure 7: Velocity profiles for the Lid-Driven Cavity Test, for a pseudoplastic with $n=0.5$

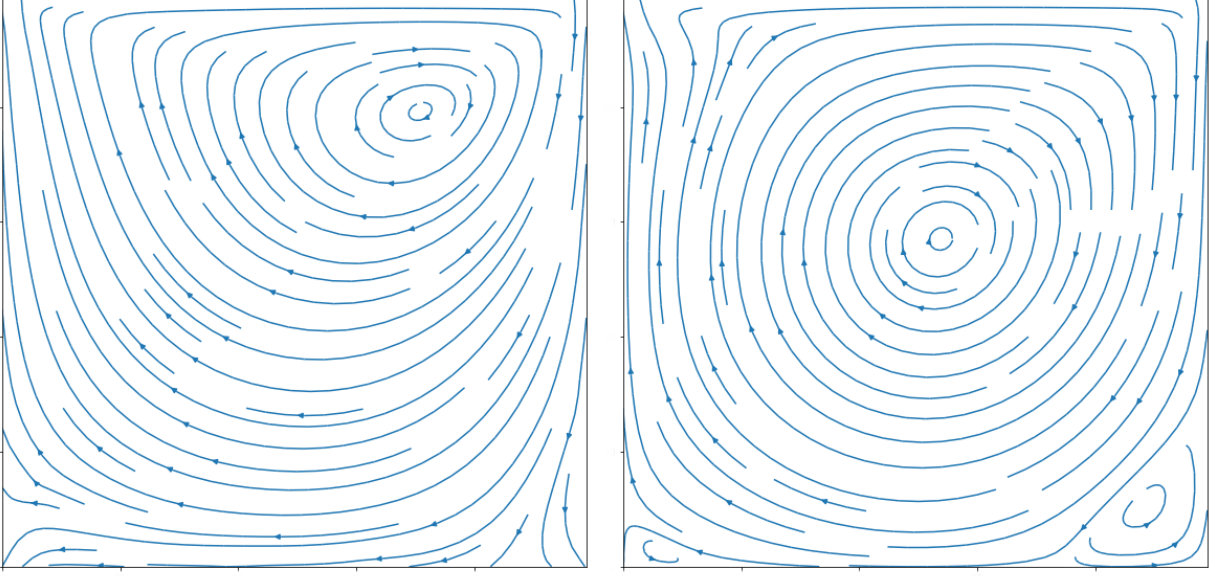


Figure 8: Streamplots for the Lid-Driven Cavity Test, for a pseudoplastic with $n=0.5$ (left) and a dilatant with $n=1.5$ (right)

by a plastic shock wave. The following parameters were used: $\rho_0 = 8930$, $c_s = 2244$, $\sigma_0 = 9 \times 10^7$, $\tau_0 = 1$. The shock Mie-Gruneisen EOS is used for the internal energy, with $p_0 = 0$, $c_0 = 3940$, $\Gamma_0 = 2$, $s = 1.48$. Figure 9 on page 21 demonstrates the results using the split solver for various values of n . These results are compared with the exact solution to the problem under perfect plasticity (to which the former results should converge as $n \rightarrow \infty$). The nature of the split solver enables large values of n to be used, producing more accurate results than those found in Peshkov et al. [20]. 400 grid cells were used, with a third order WENO method.

4.5. Cylindrical Shock

This test is taken from Barton et al. [2]. It consists of a slab of copper, occupying the domain $[0, 20]^2$, initially at rest. The region $r \leq 2$ is at ambient conditions, with zero pressure. The region $r > 2$ is at raised pressure 10^{10} and temperature 600.

The simulation is run to $t = 10^{-5}$ on a grid of shape 500×500 . A third order WENO scheme is used, with a CFL number of 0.8. The resulting radial density and velocity profiles are given in Figure 10 on page 22. The results are compared with those of the 1D radially-symmetric scheme found in Barton et al. [2], which are in turn compared with the 2D results from the same publication. As can be seen, the 2D results computed using the new split solver for the GPR model more closely match the 1D radially-symmetric results than the 2D results from the aforementioned publication, with the spikes in both variables around $r = 2$ and the wave around $r = 6$ being more accurately resolved. The 2D heatmaps of density and speed are given in Figure 11 on page 22.

5. Conclusions

In summary, a means of modeling power-law dilatants and pseudoplastics under the GPR model has been presented. A new numerical method - based on an operator splitting combined with some analytical results - has also been presented for solving this version of the GPR model, and this numerical method has been applied also to the case of elastoplastic solids under a power-law plasticity model.

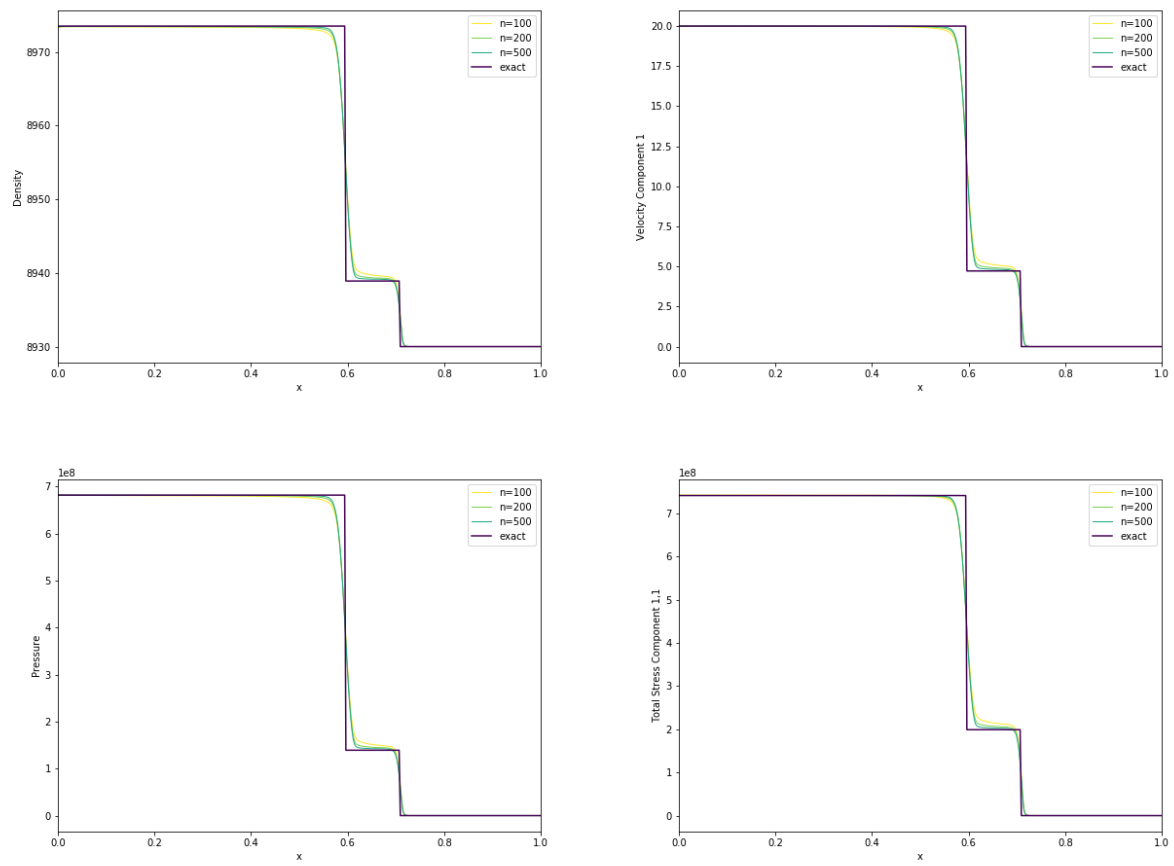


Figure 9: Density, velocity, pressure, and total stress in the elastoplastic piston test

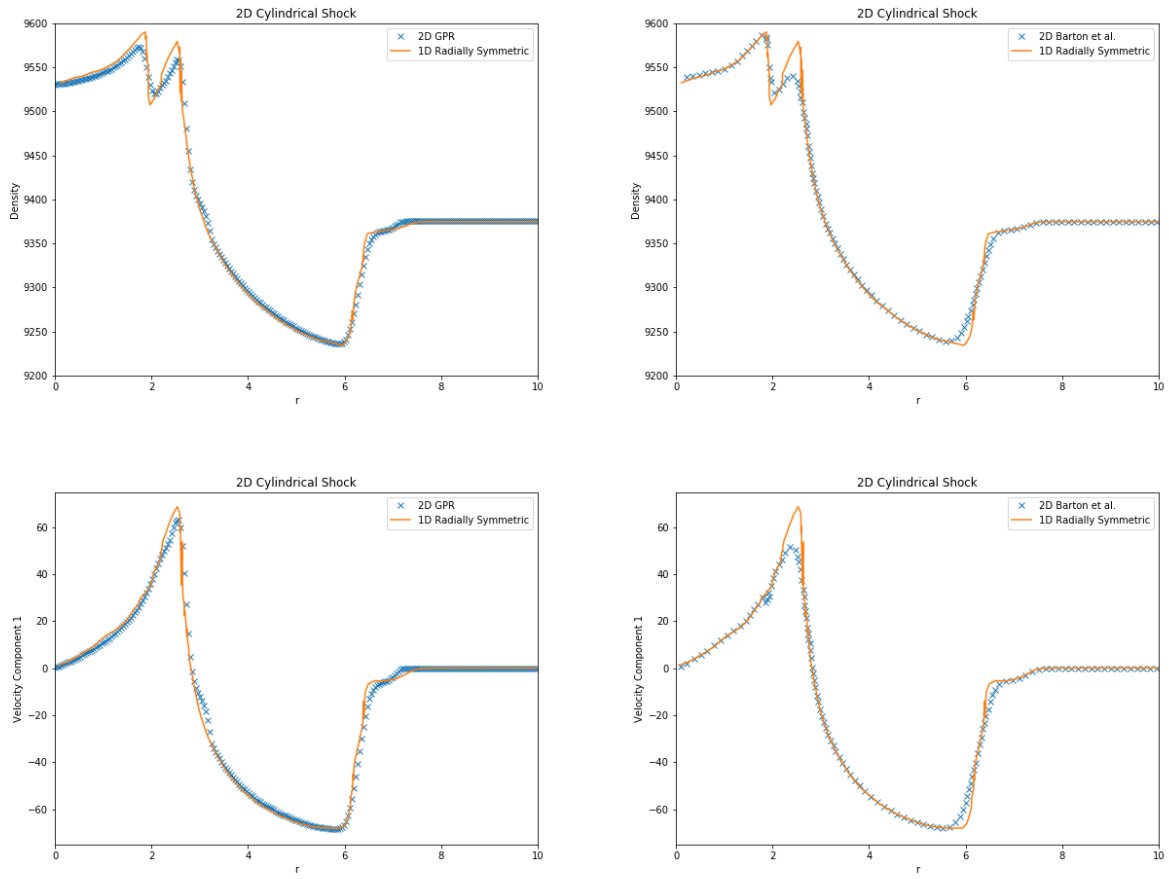


Figure 10: Density and velocity for the Cylindrical Shock Test, comparing the GPR model (left) with the model from Barton et al. [2] (right)

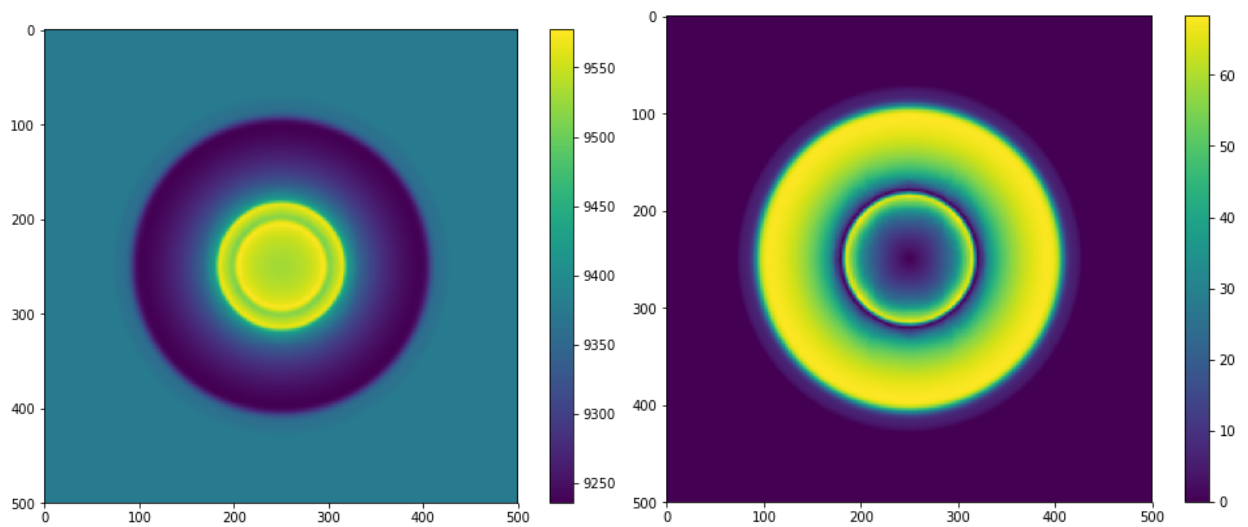


Figure 11: 2D plots of density and speed for the Cylindrical Shock Test

It should be noted that the operator splitting method presented here will inevitably suffer from the incorrect speed of propagation of discontinuities on regular, structured grids. This is due to a lack of spatial resolution in evaluating the source terms, as detailed in Leveque and Yee [15]. This issue can be rectified by the use of some form of shock tracking or mesh refinement, as noted in the cited paper. It is noted in Dumbser et al. [5] that operator splitting-based methods can result in schemes that are neither well-balanced nor asymptotically consistent. The extent to which these two conditions are violated by this method – and the severity in practice of any potential violation – is a topic of further research.

It should be noted that the assumption (53) used to derive the approximate analytical solver may break down for situations where the flow is compressed heavily in one direction but not the others. The reason for this is that one of the singular values of the distortion tensor will be much larger than the others, and the mean of the squares of the singular values will not be close to its geometric mean, meaning that the subsequent linearization of the ODE governing the mean of the singular values fails. It should be noted that none of the situations covered in this study presented problems for the approximate analytical solver, and situations which may be problematic are in some sense unusual. In any case, a stiff ODE solver can be used to solve the systems (22a), (22b) if necessary, and so this method is still very much usable in these situations, albeit slightly slower.

It should be noted that this method, as described in this study, are trivially parallelizable on a cell-wise basis. Thus, given a large number of computational cores, deficiencies in this method in terms of its order of accuracy may be overcome by utilizing a larger number of computational cells and cores. The number of grid cells that can be used scales roughly linearly with number of cores, at constant time per iteration.

6. References

- [1] Barton, P. T., Drikakis, D., Romenski, E., Titarev, V. a., 2009. Exact and approximate solutions of Riemann problems in non-linear elasticity. *Journal of Computational Physics* 228 (18), 7046–7068.
- [2] Barton, P. T., Drikakis, D., Romenski, E. I., 2011. An Eulerian finite-volume scheme for large elastoplastic deformations in solids. *International Journal for Numerical Methods in Engineering* 81, 453–484.
- [3] Bell, B. C., Surana, K. S., Jan. 1994. p-version least squares finite element formulation for two-dimensional, incompressible, non-Newtonian isothermal and non-isothermal fluid flow. *International Journal for Numerical Methods in Fluids* 18 (2), 127–162.
- [4] Boscheri, W., Dumbser, M., Loubere, R., 2016. Cell centered direct Arbitrary-Lagrangian-Eulerian ADER-WENO finite volume schemes for nonlinear hyperelasticity. *Computers and Fluids* 134–135, 111–129.
- [5] Dumbser, M., Enaux, C., Toro, E. F., 2008. Finite volume schemes of very high order of accuracy for stiff hyperbolic balance laws. *Journal of Computational Physics* 227 (8), 3971–4001.
- [6] Dumbser, M., Peshkov, I., Romenski, E., Zanotti, O., 2015. High order ADER schemes for a unified first order hyperbolic formulation of continuum mechanics: viscous heat-conducting fluids and elastic solids. *Journal of Computational Physics* 314, 824–862.
- [7] Dumbser, M., Peshkov, I., Romenski, E., Zanotti, O., 2016. High order ADER schemes for a unified first order hyperbolic formulation of Newtonian continuum mechanics coupled with electro-dynamics.
- [8] Dumbser, M., Toro, E. F., 2011. On universal Osher-type schemes for general nonlinear hyperbolic conservation laws. *Communications in Computational Physics* 10 (3), 635–671.
- [9] Dumbser, M., Toro, E. F., 2011. A simple extension of the Osher Riemann solver to non-conservative hyperbolic systems. *Journal of Scientific Computing* 48 (1-3), 70–88.
- [10] Dumbser, M., Zanotti, O., Hidalgo, A., Balsara, D. S., 2013. ADER-WENO finite volume schemes with space-time adaptive mesh refinement. *Journal of Computational Physics* 248, 257–286.
- [11] Ferras, L. L., Nobrega, J. M., Pinho, F. T., 2012. Analytical solutions for Newtonian and inelastic non-Newtonian flows with wall slip. *Journal of Non-Newtonian Fluid Mechanics* 175–176, 76–88.
- [12] Frenkel, J., 1947. *Kinetic Theory of Liquids*. Oxford University Press.
- [13] Giles, M. B., 2008. An extended collection of matrix derivative results for forward and reverse mode algorithmic differentiation. Tech. Rep. 9783540689355.
URL <http://eprints.maths.ox.ac.uk/1079/>
- [14] Jackson, H., 2017. A Fast Numerical Scheme for the Godunov-Peshkov-Romenski Model of Continuum Mechanics. *Journal of Computational Physics* 348, 514–533.
URL <http://dx.doi.org/10.1016/j.jcp.2017.07.055>
- [15] Leveque, R., Yee, H., 1990. A Study of Numerical Methods for Hyperbolic Conservation Laws with Stiff Source Terms. *Journal of Computational Physics* 86, 187–210.

- [16] Maire, P. H., Abgrall, R., Breil, J., Loubere, R., Rebourecet, B., 2013. A nominally second-order cell-centered Lagrangian scheme for simulating elastic-plastic flows on two-dimensional unstructured grids. *Journal of Computational Physics* 235, 626–665.
- [17] Malyshev, A. N., Romenskii, E. I., 1986. Hyperbolic equations for heat transfer. Global solvability of the Cauchy problem. *Siberian Mathematical Journal* 27 (5), 734–740.
- [18] McAdams, A., Selle, A., Tamstorf, R., Teran, J., Sifakis, E., 2011. Computing the Singular Value Decomposition of 3×3 matrices with minimal branching and elementary floating point operations. University of Wisconsin Madison.
- [19] Neofytou, P., May 2005. A 3rd order upwind finite volume method for generalised Newtonian fluid flows. *Advances in Engineering Software* 36, 664–680.
URL <https://dl.acm.org/citation.cfm?id=1276040.1276043>
- [20] Peshkov, I., Boscheri, W., LoubĚre, R., Romenski, E., Dumbser, M., Jun. 2018. Theoretical and numerical comparison of hyperelastic and hypoelastic formulations for Eulerian non-linear elastoplasticity. arXiv:1806.00706 [physics]ArXiv: 1806.00706.
URL <http://arxiv.org/abs/1806.00706>
- [21] Peshkov, I., Romenski, E., 2016. A hyperbolic model for viscous Newtonian flows. *Continuum Mechanics and Thermodynamics* 28 (1-2), 85–104.
- [22] Peshkov, I., Romenski, E., Dumbser, M., 2017. A unified hyperbolic formulation for viscous fluids and elastoplastic solids. URL <http://arxiv.org/abs/1705.02151>
- [23] Peshkov, I., Romenski, E., Dumbser, M., Fambri, F., 2018. General Relativistic formulation of dissipative continuum mechanics.
- [24] Romenski, E., Drikakis, D., Toro, E., 2010. Conservative models and numerical methods for compressible two-phase flow. *Journal of Scientific Computing* 42 (1), 68–95.
- [25] Romenski, E., Resnyansky, A. D., Toro, E. F., 2007. Conservative hyperbolic model for compressible two-phase flow with different phase pressures and temperatures. *Quarterly of applied mathematics* 65(2) (2), 259–279.
- [26] Romenski, E. I., 1989. Hyperbolic equations of Maxwell’s nonlinear model of elastoplastic heat-conducting media. *Siberian Mathematical Journal* 30 (4), 606–625.
- [27] Sverdrup, K., Nikiforakis, N., Almgren, A., Sep. 2018. Highly parallelisable simulations of time-dependent viscoplastic fluid flow with structured adaptive mesh refinement. *Physics of Fluids* 30 (9), 093102.
- [28] Toro, E. F., 2009. *Reimann Solvers and Numerical Methods for fluid dynamics*. Vol. 40.

7. Acknowledgments

I acknowledge financial support from the EPSRC Centre for Doctoral Training in Computational Methods for Materials Science under grant EP/L015552/1.